Available online at www.sciencedirect.com
ScienceDirect
Trans. Nonferrous Met. Soc. China 34(2024) 2138−2152
Transactions of Nonferrous Metals Society of China
www.tnmsc.cn

Effect of deformation temperature on microstructure and texture of AZ31 magnesium alloy processed by new plastic deformation method

Yu-tian FAN[1], Li-wei LU[1,2], Jian-bo LIU[1], Min MA[1,2], Wei-ying HUANG[2,3], Rui-zhi WU[2,4]

1. School of Materials Science and Engineering, Hunan University of Science and Technology, Xiangtan 411201, China;
2. Hunan Jinfeng Mechanical Technology Co., Ltd., Loudi 417700, China;
3. Key Laboratory of Efficient & Clean Energy Utilization, School of Energy and Power Engineering, Changsha University of Science & Technology, Changsha 410114, China;
4. Key Laboratory of Superlight Material and Surface Technology, Ministry of Education, College of Materials Science and Chemical Engineering, Harbin Engineering University, Harbin 150001, China

Received 1 January 2023; accepted 13 June 2023

Abstract: A new method of repeated upsetting−extrusion (RUE) deformation was presented. The effects of different deformation temperatures on the microstructure and texture of RUE deformed AZ31 magnesium (Mg) alloy were studied using optical microscopy (OM), X-ray diffraction (XRD), electron backscatter diffraction (EBSD), and Vickers hardness tester. The results show that the microstructure of the AZ31 Mg alloy is locally refined to 0.8 μm after RUE deformation, and the main refinement mechanism is the continuous dynamic recrystallization (CDRX). As the temperature increases, the texture of basal plane parallel to shearing plane is formed firstly, followed by $\{11\bar{2}0\}\langle 10\bar{1}0\rangle$ texture with weaker intensity, and finally $\{0001\}\langle 10\bar{1}0\rangle$ and $\{0001\}\langle 11\bar{2}0\rangle$ textures. The texture split is caused by the dislocation slip of basal $\langle a\rangle$ and pyramidal $\langle a\rangle$. The maximum hardness of the AZ31 Mg alloy after RUE deformation is increased by 42.4% compared with that at the initial state, which is mainly due to the fine-grained strengthening and the dislocation strengthening.

Key words: AZ31 Mg alloy; repeated upsetting−extrusion; dynamic recrystallization; texture; hardness

1 Introduction

Mg alloys, with low density, high specific strength and stiffness, easy recycling, and superior machinability, are important lightweight structural materials with broad market demand in the fields of aerospace, transportation, and 3C electronic products [1]. However, due to the hexagonal close-packed (HCP) structure of Mg alloys, this crystallographic structure determines a limited number of slip systems that can be activated at room temperature, which severely restricts the application range of Mg alloys [2].

Grain refinement is an effective method for synergistically improving the strength and plasticity of Mg alloys. Numerous studies have illuminated that severe plastic deformation (SPD) technologies can effectively refine grains and improve the mechanical properties of Mg alloys [3]. Currently, the main SPD technologies include accumulative roll bonding (ARB) [4], high-pressure torsion (HPT) [5], multi-direction forging (MDF) [6], equal channel angular pressing (ECAP) [7], and cyclic

Corresponding author: Li-wei LU, Tel: +86-17773201878, E-mail: cqulqyz@126.com;
Rui-zhi WU, Tel: +86-13074559355, E-mail: rzwu@hrbeu.edu.cn
DOI: 10.1016/S1003-6326(24)66530-1

extrusion compression (CEC) [8], etc. CHENG et al [9] performed 8 passes of ECAP on the Mg−8Sn−6Zn−2Al alloy at 300 °C. When increasing from 2 to 6 passes, the grains showed obvious dynamic recrystallization behavior, with the recrystallization fraction reaching approximately 91% and the average grain size decreasing to 2.49 μm, but the grains grew to 3.07 μm after extrusion for 8 passes. JI et al [10] proposed a cyclic expansion extrusion with an asymmetrical extrusion cavity (CEE-AEC) technique, and after 3 passes of extrusion deformation, Mg alloys with uniform and fine microstructures and excellent overall mechanical properties were successfully obtained. SIAHSARANI et al [11] investigated the micro-structural evolution and mechanical properties of AZ91 Mg alloy using elevated temperature hydrostatic cyclic expansion extrusion (HCEE), which produced ultra-long, ultra-fine-grained rods with superior mechanical properties.

Although the previously mentioned SPD technology could successfully improve the internal microstructure and mechanical properties of Mg alloy, the degree of grain refinement was limited. Therefore, a new process of repeated upsetting−extrusion (RUE) deformation of Mg alloy is proposed in this research. During this process, the Mg alloy undergoes repeated radial and axial shortening or elongation by shearing, upsetting, and expansion to repeatedly deform into the initial billet size and achieve large plastic deformation. Compared to other SPD processes, RUE has greater strain in a single pass and higher deformation efficiency due to its multiple deformation characteristics. Moreover, the Mg alloy was always under two-way or three-way compressive stress during RUE processing, which prevented the Mg alloy from bending, cracking, and other defects, making the material more dense, so the process was ideal for hard-to-deform materials. As a result of the interaction of positive stress and shearing, Mg alloys continually accumulate uniform strain, refining the grain and weakening the texture to enhance strength and toughness. In this work, AZ31 Mg alloy was used as the study object to investigate the effect of deformation temperatures on the microstructure and texture of Mg alloy after RUE deformation, which offers significant theoretical reference and process guidance for the processing and production of high-performance magnesium alloy.

2 Experimental

The as-cast AZ31 Mg alloy was chosen as the experimental material. Table 1 shows the chemical composition of the experimental alloy. A rectangular billet with dimensions of 20 mm × 20 mm × 40 mm was wire cut from the AZ31 bars to perform the RUE experiments. The schematic diagram of the repeated upsetting−extrusion die is shown in Fig. 1. The RUE die consists of three parts: the convex die, the billet, and the concave die. First, a billet with a cross-sectional length and width of *I* and *D* is put into the upper cavity. As the convex die extrudes downward, the billet is laterally deformed through the interaction with the convex and concave dies until it fills the lower cavity and completes the extrusion, resulting in the length and

Table 1 Chemical composition of AZ31 alloy (wt.%)

Al	Zn	Mn	Fe	Si	Cu	S	Mg
3.00	0.90	0.26	0.04	0.07	0.03	0.03	Bal.

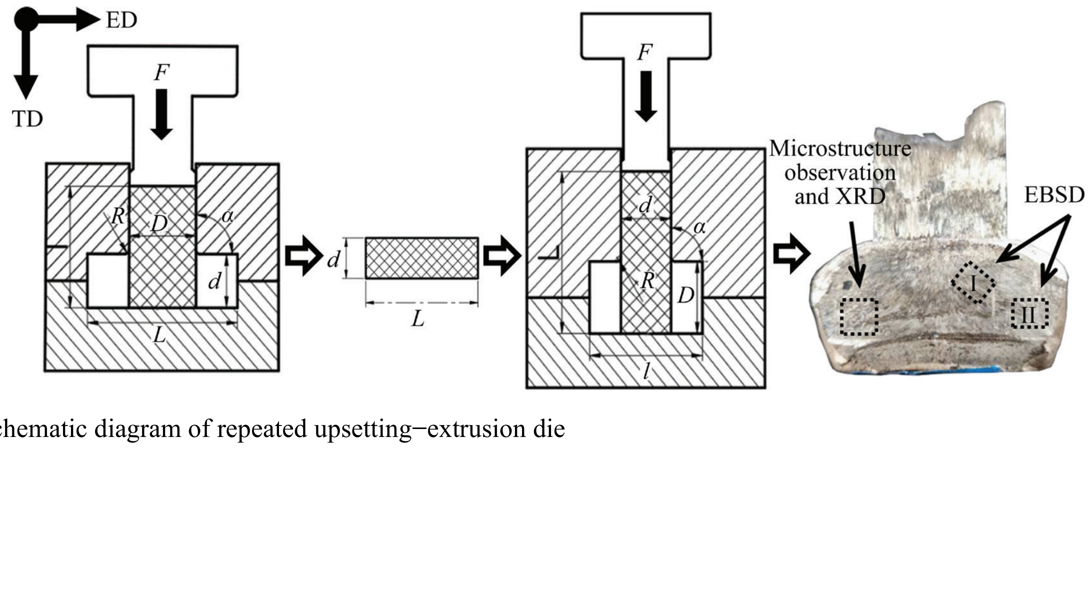

Fig. 1 Schematic diagram of repeated upsetting−extrusion die

width of the billet cross-sections becoming *L* and *d*. The billet is then rotated 90° into the second die for a second extrusion, and the dimensions of the billet cross-section change again to *I* and *D*. One cycle is defined as one deformation pass. During the deformation process, the billet is constantly subjected to shearing, upsetting, and expansion deformations.

The dies and materials were heated to 290, 350, and 410 °C in a resistance furnace and held for a period of time before the experiments. One pass RUE experiments were performed at three different temperatures to compare the effect of RUE at different temperatures on grain refinement and the improvement of the mechanical properties of AZ31 Mg alloy. Sampling was done from the center of each deformed sample, and their longitudinally sectioned surfaces were observed. Figure 1 shows the locations of these samples.

The microstructure and macro-texture of the initial states and RUEed specimens were observed along the extrusion direction (ED)−transverse direction (TD) plane using OM, XRD, and EBSD. For OM observation, the samples were etched in a solution of 1 g of oxalic acid, 1 mL of nitric acid, and 98 mL of distilled water for 25−35 s. By using Cu K radiation at a voltage of 40 kV and a current of 40 mA, XRD (XPert MRD) was used to analyze the macro-texture. The incomplete polar figures of $\{0002\}$, $\{10\bar{1}0\}$, $\{10\bar{1}1\}$ and $\{10\bar{1}2\}$ were swept in 5° step size by concentric circles, with the measurement ranges of α (0°−70°) and β (0°−360°). The EBSD sample was created using an ion beam thinner after mechanical grinding and polishing. The samples were run at 20 kV while being inclined 70° along the horizontal plane. It is set at 0.4 μm for the step size. EBSD data were processed by Channel 5 software. The hardness of the Mg alloy was studied and analyzed by using a Vickers hardness tester to test the sample at eight points. The loading load and loading time for the hardness test were 5 N and 10 s, respectively.

3 Results and discussion

3.1 Microstructure

Figure 2 shows the microstructure of the AZ31 Mg alloy in different states. It can be seen from Fig. 2(a) that the grains of the AZ31 Mg alloy in the initial state are relatively coarse, with an average grain size of approximately 276.8 μm. After RUE deformation at 290 °C, there are a large number of initial grains without dynamic recrystallization (DRX) and a large number of broken fine grains in the microstructure, as shown in Fig. 2(b). The dynamic recovery process is slow due to the low stacking fault energy and wide extended dislocations of Mg, which are difficult to unwind from nodes and dislocation networks and also difficult to make dissimilar dislocations cancel each other by cross-slipping and climbing [12]. The dislocation density in the substructure is high, and the large strain causes the grains to break beyond the critical deformation level. In addition, the strain generated by deformation can provide sufficient driving force for DRX, and the dislocations accumulated on the subgrain boundaries are absorbed to accelerate the process of DRX, resulting in the formation of a large number of finely equiaxed recrystallized grains along the grain boundaries. Furthermore, Fig. 2(e) shows that the grain size distribution is scattered, the microstructure refinement is not uniform enough, some of the grains turn into long strip grains, and the broken grains do not undergo complete DRX.

Compared with 290 °C, Figs. 2(c, f) show that the overall uniformity of the deformed microstructure at 350 °C is greatly improved. The main distribution of grain size ranges from 5 to 15 μm, indicating that the Mg alloy billets undergo sufficient DRX after RUE at this temperature and that the microstructure mainly consists of a large number of finely equiaxed grains. As the deformation temperature increases (410 °C), dynamic recovery is enhanced. Under the same strain conditions, deformation is not enough to provide sufficient energy for DRX, resulting in insufficient DRX. It can be seen from Fig. 2(d) that there are not only fine grains with a grain size of approximately 2 μm, but also coarse initial grains larger than 25 μm, showing a typical bimodal grain structure. As shown in Fig. 2(g), the proportion of grains smaller than 5 μm increases, while the proportion of grains larger than 15 μm also increases compared to Figs. 2(e, f), and the uniformity of the grains is lower.

3.2 Macro-texture

The (0002) and $(10\bar{1}0)$ pole figures of different samples are shown in Fig. 3. In the (0002)

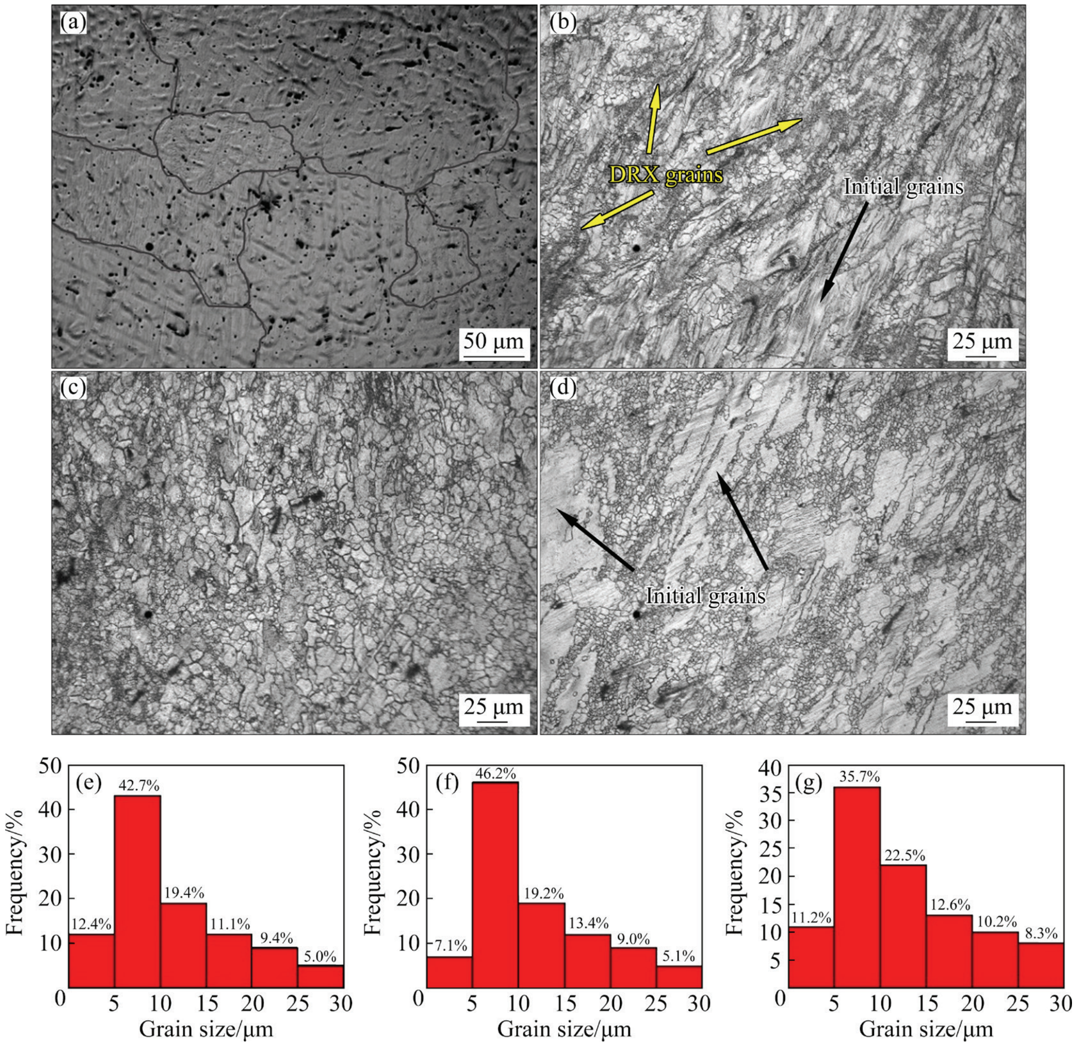

Fig. 2 Microstructure and grain size distribution of AZ31 alloy in different states: (a) As-cast sample; (b, e) RUE at 290 °C; (c, f) RUT at 350 °C; (d, g) RUE at 410 °C

pole figure, the peak texture components are located at both ends of the TD for AZ31 Mg alloy samples extruded at 290 and 350 °C, while there are four peak texture components along the ED in the $(10\overline{1}0)$ pole figure. This indicates that at these two extrusion temperatures, the AZ31 Mg alloy exhibits a typical non-basal fiber texture with mainly pyramidal orientation characteristics. Most of the grains are oriented parallel to the shearing plane after corner shearing deformation, and the weak effect of upsetting deformation allows them to maintain this fiber texture.

As temperature increases, the peak intensity of the (0002) pole figure decreases from 6.1 to 4.3, and the peak intensity of the $(10\overline{1}0)$ pole figure decreases from 2.3 to 2. At 350 °C, the (0002) pole figure texture axis is deflected approximately 5° around the normal direction (ND), and a weak intensity basal texture begins to appear. The $(10\overline{1}0)$ pole figure texture axis is also deflected around the ND, and the primary and secondary intensity peaks are interchanged with a more diffusive distribution. In a study of the effect of three different paths of ECAP on the texture of AX41 Mg alloy, KRAJŇÁK et al [13] found partial differences in the (0001) pole figures for grains smaller and larger than 2 μm, even for samples that underwent one pass of deformation under the same path. The increase in temperature accelerates the DRX, and the orientation changes after the coarse grains are divided into fine recrystallized grains. At the same time, the pyramidal slip system is activated by the increase in temperature [14], enhancing the rotation of the c-axis so that the basal plane is more susceptible to deflection by upsetting action.

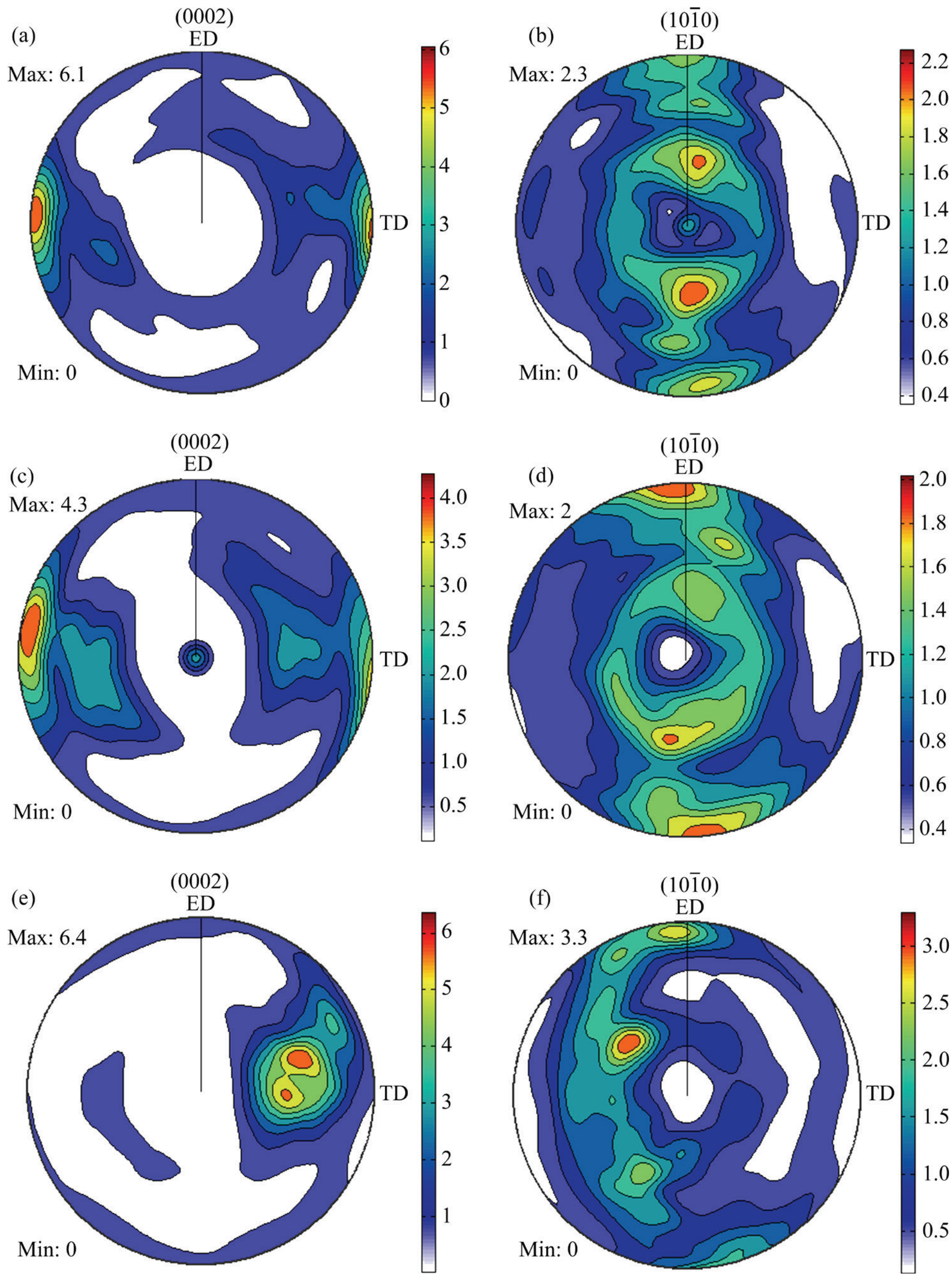

Fig. 3 (0002) and (10$\bar{1}$0) pole figures of samples after RUE deformation at different temperatures: (a, b) 290 °C; (c, d) 350 °C; (e, f) 410 °C

The (0002) and (10$\bar{1}$0) pole figures at 410 °C are shown in Figs. 3(e, f), and the texture components change considerably at this time. The pole density point in the (0002) pole figure is deflected approximately 20° toward the center, indicating that the *c*-axis turns approximately 20° around the ND, while the basal texture in the 350 °C pole figure disappears. However, the peak intensities of the (0002) and (10$\bar{1}$0) pole figures increase further, from 4.3 to 6.4 and from 2 to 3.3, respectively. At 410 °C, due to insufficient DRX, there are still coarse initial grains in the microstructure, forming a new texture. WU et al [15] rolled AZ31B Mg alloy at 773 K and found that the {0001} texture completely disappeared and a {05$\bar{5}$2} + {01$\bar{1}$0} texture was formed, and showed that the formation of this texture was caused by slip and twinning at high temperature.

Figures 4(a−c) depict orientation distribution function (ODF) of the AZ31 Mg alloy at φ_2=0° and φ_2=30°, which corresponds to the pole figure of Fig. 3. Two characteristic fiber texture components, {11$\bar{2}$0}⟨10$\bar{1}$0⟩ and {10$\bar{1}$0}⟨11$\bar{2}$0⟩, exist in the AZ31 Mg alloy at 290 °C (Fig. 4(a)), with peak Euler angles of (36°, 85°, 0°) and (38°, 89°, 30°) and texture intensities of 4.1 and 2.9, respectively. The main texture component is the $\{11\bar{2}0\}\langle 10\bar{1}0\rangle$ fiber texture, which means that most of the grains have pyramidal planes parallel to ED and the crystal orientation is at an angle of approximately 36° to the TD. As the temperature increases to 350 °C (Fig. 4(b)), the peak Euler angles change to (20°, 80°, 0°), closer to the ideal $\{11\bar{2}0\}\langle 10\bar{1}0\rangle$ position with a more diffusive distribution, and the intensity decreases from 4.1 to 3.6. The $\{10\bar{1}0\}\langle 11\bar{2}0\rangle$ texture component disappears and begins to show a $\{0001\}\langle 10\bar{1}0\rangle$ basal texture with an intensity of 2.6 and the presence of a few crystals of $\langle 11\bar{2}0\rangle$ parallel to TD. The temperature continues to increase to 410 °C, at which the strongest point of the texture density

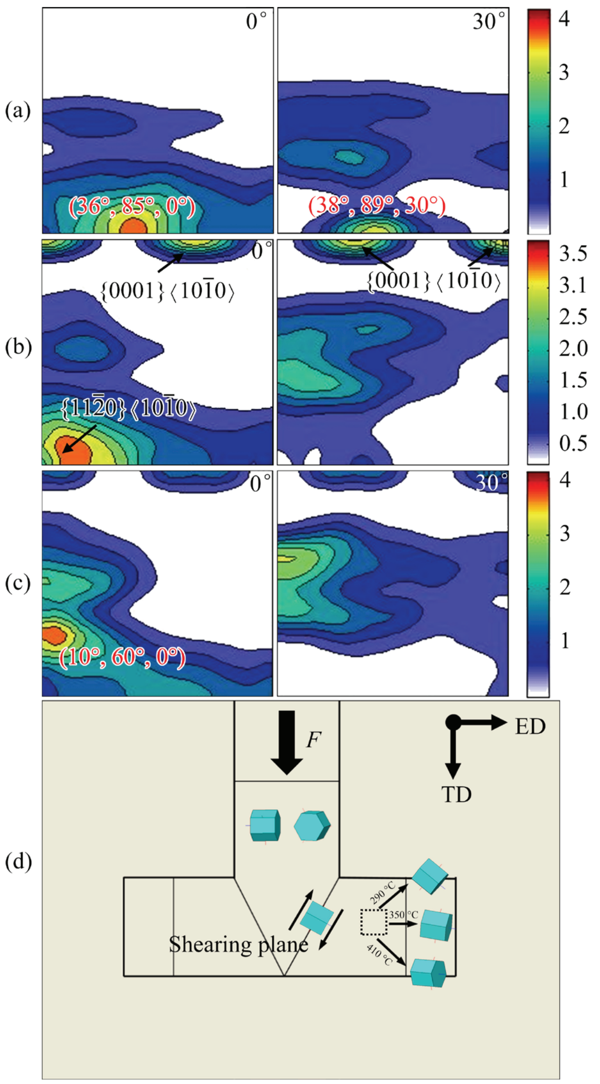

Fig. 4 ODF (φ_2=0° and φ_2=30°) (a−c) of RUEed samples at 290 °C (a), 350 °C (b), and 410 °C (c) and schematic diagram of macro-texture evolution (d)

shifts from Φ=80° to Φ=60°, i.e., most of the grains deflect 20° around the ED, as shown in Fig. 4(c). The texture intensity increases to 4.3, while the basal texture $\{0001\}\langle 10\bar{1}0\rangle$ intensity weakens and transforms to $\langle 11\bar{2}0\rangle$ parallel to ED.

In brief, different deformation temperatures cause changes in both the texture components and intensity of the AZ31 Mg alloy after RUE deformation. Figure 4(d) shows a schematic diagram of the macro-texture evolution of the RUEed alloy at different temperatures. The billets used for RUE deformation are prepared from bar cuts and have a typical basal fiber texture. The deformation process results in the formation of a shear band due to the corner shearing action, and after the corner shearing deformation, the slip system within the alloy is fully activated, resulting in the orientation of the basal plane parallel to the shearing plane [16]. As the temperature increases, the non-basal slip system is activated and the grains are more susceptible to rotation, with the $\{11\bar{2}0\}\langle 10\bar{1}0\rangle$ texture being closer to the ideal position at 350 °C compared to 290 °C. The formation of $\{0001\}\langle 10\bar{1}0\rangle$ and $\{0001\}\langle 11\bar{2}0\rangle$ orientation dominance when the temperature is further increased to 410 °C may then be caused by different slip modes and specially oriented grains.

3.3 EBSD results

In order to further investigate the refinement mechanism of RUE deformation on the micro-structure of Mg alloy, EBSD was used to analyze the information related to the microstructure of Mg alloy at 290 °C. The inverse pole figure (IPF) maps of different deformation zones and their corresponding misorientation angle distribution are shown in Fig. 5. The gray lines in the maps represent grain boundaries with misorientation angles ranging from 2° to 15°, commonly known as low-angle grain boundaries (LAGBs), while the black lines represent high-angle grain boundaries (HAGBs) with misorientation angles larger than 15°.

From Figs. 5(a, b), it can be seen that the color of the grains varies when they are in the initial stage of deformation, which indicates that the grain orientation of AZ31 Mg alloy is random in Zone I and that the grain size of the alloy is significantly refined to approximately 12.4 μm. After that, the billet continues to be deformed, the grains start to

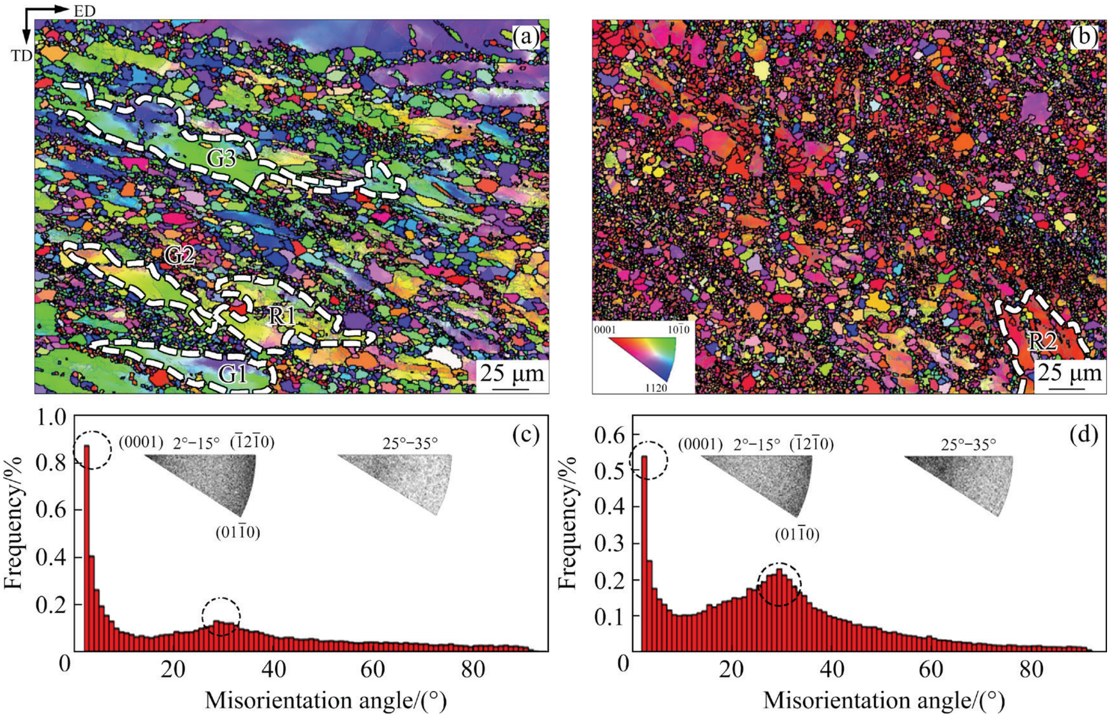

Fig. 5 Inverse pole figure maps (a, b) and distribution histogram of misorientation angle with axis distributions for angles of 2°−15° and 25°−35° (c, d): (a, c) Zone I; (b, d) Zone II

exhibit expansion deformation after corner shearing and upsetting deformation, and the large grains are obviously reduced when entering Zone II. The average grain size is about 7.8 μm, and the local area is refined to be 0.8 μm. TIAN et al [17] performed a tube continuous extrusion−shear−expanding (TCESE) deformation of AZ31 Mg alloy, and the grain size of AZ31 Mg alloy was only reduced to 10 μm. This demonstrates the superiority of RUE deformation in grain refinement. In addition, it can be clearly seen from Fig. 5(a) that there are many LAGBs within the coarse grains, which are caused by a large number of dislocations and rapid climbing. With continuous deformation, the LAGBs absorb moving dislocations and transform into HAGBs, and the coarse grains are segmented continuously. It is inferred that there is a CDRX mechanism during RUE deformation.

Figures 5(c, d) show the distribution of misorientation angles in different regions, showing two peaks in the range of LAGBs (2°−15°) and 25°−35°. The LAGBs show no obvious axis of rotation. It is worth noting that the peak of the misorientation angle in the range of 25°−35° increases significantly with increasing deformation degree. According to previous studies, the recrystallization and grain growth of metal materials with HCP structures often lead to a *c*-axis rotation of 25°−35° [18]. This indicates that the high peak values in the vicinity of 25°−35° may be due to the DRX process or grain growth during extrusion deformation.

Figures 6(a, b) show the distribution of dynamic recrystallization (DRX) in the Mg alloy during deformation, with red, yellow, and blue representing deformed grains, subgrains, and dynamically recrystallized grains, respectively. At the initial deformation stage (Fig. 6(a)), the deformation degree of Mg alloy is small, the microstructure is dominated by deformed grains, and there are some DRXed grains and subgrains. Some DRXed grains can be observed at the grain boundaries of larger grains. With the process of RUE deformation (Fig. 6(b)), most of the subgrains disappear after deformation, and the grains evolve into refined deformed grains and tiny recrystallized grains, as well as more crushed fine crystal structures. With the progress of extrusion deformation, the DRX becomes increasingly sufficient, and the DRX grains of Mg alloys gradually increase, from the initial 36% to 47% (Fig. 6(c)).

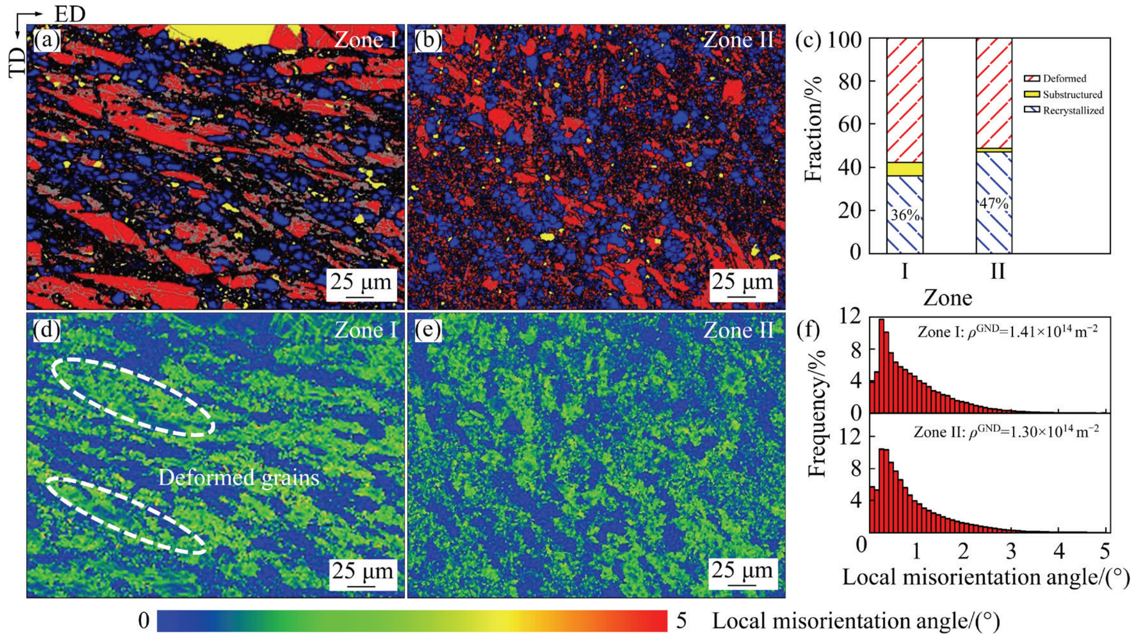

Fig. 6 Recrystallization grain distribution map (a, b) and corresponding recrystallization fraction map (c); KAM maps (d, e) and corresponding KAM relative frequency (f)

The driving force of recrystallization is the deformation storage energy that is not released after recovery. The nucleation mechanisms include grain boundary bowing out mechanism, subgrain migration mechanism, and subgrain merging mechanism [19]. The misorientation angle between adjacent grains increases further after recrystallization, resulting in an HAGB (>15°). Therefore, the degree of recrystallization or recovery of the material can be qualitatively analyzed by using the kernel average misorientation (KAM), and then the geometric dislocation density during deformation can be quantitatively analyzed by Eq. (1) [20] and Eq. (2) [21], as shown in Figs. 6(d−f). With continuous deformation, the strain continuously accumulates, a large number of dislocations entangle in the deformed grains, and the dynamically recrystallized grains nucleate more and refine the grains. At the same time, the large plastic deformation leads to an intensification of lattice distortion and many recrystallization nucleations. The continuous generation of new DRX grains causes the gradual change in color inside the grains to blue. This shows that the dislocation density in the grains is small and that there is no obvious stress concentration at this time. The DRX process consumes a large number of dislocations, and the dislocation density in the grains is reduced as a whole. As shown in Fig. 6(f), the geometric dislocation density from Zone I to Zone II decreases from 1.41×10^{14} to 1.30×10^{14} m^{-2}.

$$\mathrm{KAM}_{\mathrm{ave}}=\exp\left[\frac{1}{N}\sum_{1}^{i}\ln \mathrm{KAM}_i\right] \tag{1}$$

where KAM_i is the local KAM value at Point i, and N is the number of points in the test area.

$$\rho^{\mathrm{GND}}=\frac{2\mathrm{KAM}_{\mathrm{ave}}}{\mu b} \tag{2}$$

where μ is the step size, b is the length of the Bosch vector, and $\mathrm{KAM}_{\mathrm{ave}}$ is the average KAM value of the selected area.

Figure 7 shows the (0002) pole figures and inverse pole figures of samples at different deformation stages. It can be seen from Figs. 7(a, c) that the c-axis of most grains in Zone I deviates from the TD, with a pole density of 8.83, which is caused by the deflection of the c-axis under the shearing action and makes the basal plane parallel to the shearing plane. However, the distribution of grain orientation in other parts is diffuse, indicating that the grain orientation in this zone is constantly separated from the effect of shearing, and the crystal orientation of most grains parallel to ED is $\langle 10\bar{1}1\rangle$. The texture in Zone II deflects about 20° to the basal plane, and the whole is oriented to the

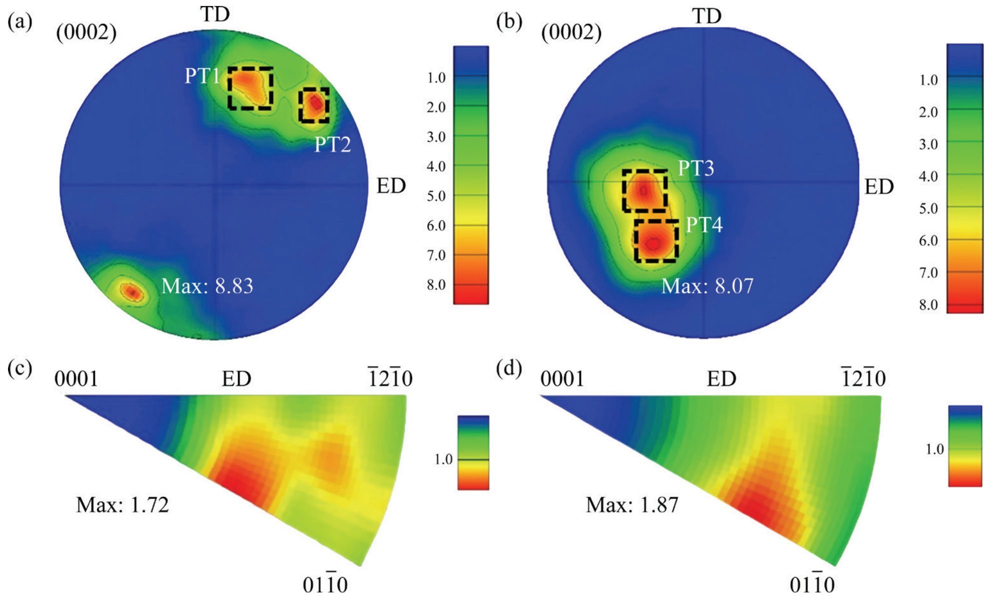

Fig. 7 (0002) pole figures (a, b) and inverse pole figures (c, d) of different zones: (a, c) Zone I; (b, d) Zone II

basal plane. With the continuous deformation, the billet is mainly affected by the upsetting deformation and expansion deformation at this stage, and the basal plane is gradually parallel to TD, forming a strong basal plane texture with a pole density of 8.07. In addition, the textures in different zones display significant splitting.

In order to analyze the cause of texture split, Schmid factor (SF) analysis was conducted on the main grains of peak texture components (PT1−PT4) in Figs. 7(a, b), as shown in Fig. 8. To examine the activation of a typical slip system, SF maps are applied: pyramidal $\langle c+a\rangle$ slip − $(11\bar{2}2)\langle 11\bar{2}\bar{3}\rangle$, pyramidal ⟨a⟩ slip− $(10\bar{1}1)\langle 1\bar{2}10\rangle$, prismatic $\langle a\rangle$ slip− $(10\bar{1}0)\langle \bar{1}2\bar{1}0\rangle$ and basal $\langle a\rangle$ slip− $(0001)\langle 11\bar{2}0\rangle$ [22]. The average SF value of several typical slip systems of the primary grains of PT1−PT4 in Figs. 7(a, b) is given in Table 2. It is obvious that the SF values of basal $\langle a\rangle$ and pyramidal $\langle a\rangle$ slip are very high, indicating that these two slip systems are fully activated during RUE deformation. According to the core mechanism of CDRX, $\langle a\rangle$ dislocations cross slip on the non-basal plane, and slip from the basal plane to the non-basal plane. Because the basal plane texture is easily formed during RUE deformation, which inhibits the SF of the prismatic slip system, the basal plane $\langle a\rangle$ dislocation slip can only slip towards the pyramidal slip system, so the SF value of the pyramidal slip system is very high. In addition, the non-basal slip system is difficult to be opened at room temperature due to the high critical resolved shear stress (CRSS). However, the CRSS of the non-basal slip system decreases significantly with increasing temperature. As a result, the combined action of basal $\langle a\rangle$ and pyramidal $\langle a\rangle$ dislocation slip is the primary cause of base texture split. Previous studies have reported that pyramidal slip may lead to the split of basal texture [23].

DRX is a crucial factor that influences grain size and orientation in Mg alloys. It is of great significance in controlling and adjusting Mg alloy structure deformation, improving plastic forming ability, and enhancing mechanical properties [24]. In order to study the DRX grain refining mechanism of the AZ31 Mg alloy during RUE deformation, three typical coarse grains (G1−G3) and two DRX regions, R1 and R2, are selected from Figs. 5(a, b) for analysis, as shown in Figs. 9 and 10.

It is obvious from Figs. 9(a−d) that G1 is composed of green and purple areas. The misorientation angle developing along the red arrow AB (Fig. 9(d)) shows that the misorientation inside the grain gradually increases until it is close to 20, which indicates that the orientation of G1 along the AB direction is constantly changing. Figures 9(b, c) show the (0002) pole figure and inverse pole figure of G1, respectively. It can be determined that the basal plane direction of the two

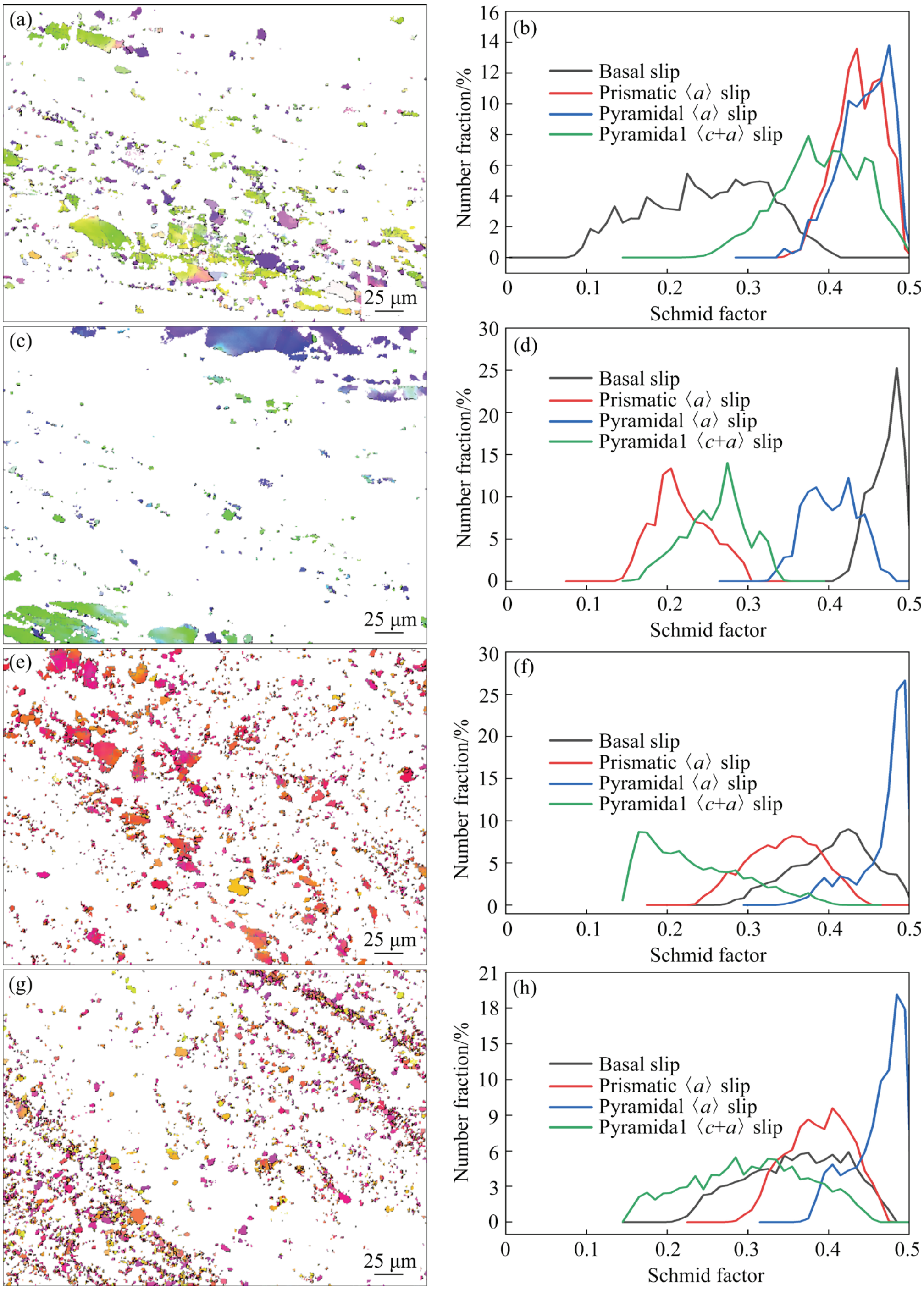

Fig. 8 Inverse pole figure (a, c, e, g) and SF distribution (b, d, f, h) of main grains of PT1 (a, b), PT2 (c, d), PT3 (e, f) and PT4 (g, h) selected in Figs. 7(a, b)

Table 2 Average SF value of different slip systems of major grains of PT1−PT4

Slip system	PT1	PT2	PT3	PT4
Basal ⟨*a*⟩ slip	0.24	0.47	0.41	0.37
Prismatic ⟨*a*⟩ slip	0.44	0.22	0.34	0.38
Pyramidal ⟨*a*⟩ slip	0.44	0.41	0.47	0.46
Pyramidal ⟨*c*+*a*⟩ slip	0.40	0.26	0.22	0.30

regions of G1 is almost the same, while the region from green to purple gradually changes to $[\bar{1}2\bar{1}4]$ parallel to ED, which can also be confirmed from the grain orientation diagram of specific points inserted along the AB direction in Fig. 9(a). In addition, there are a large number of LAGBs in G1, which are caused by the accumulation of dislocations or subgrain boundaries in deformed

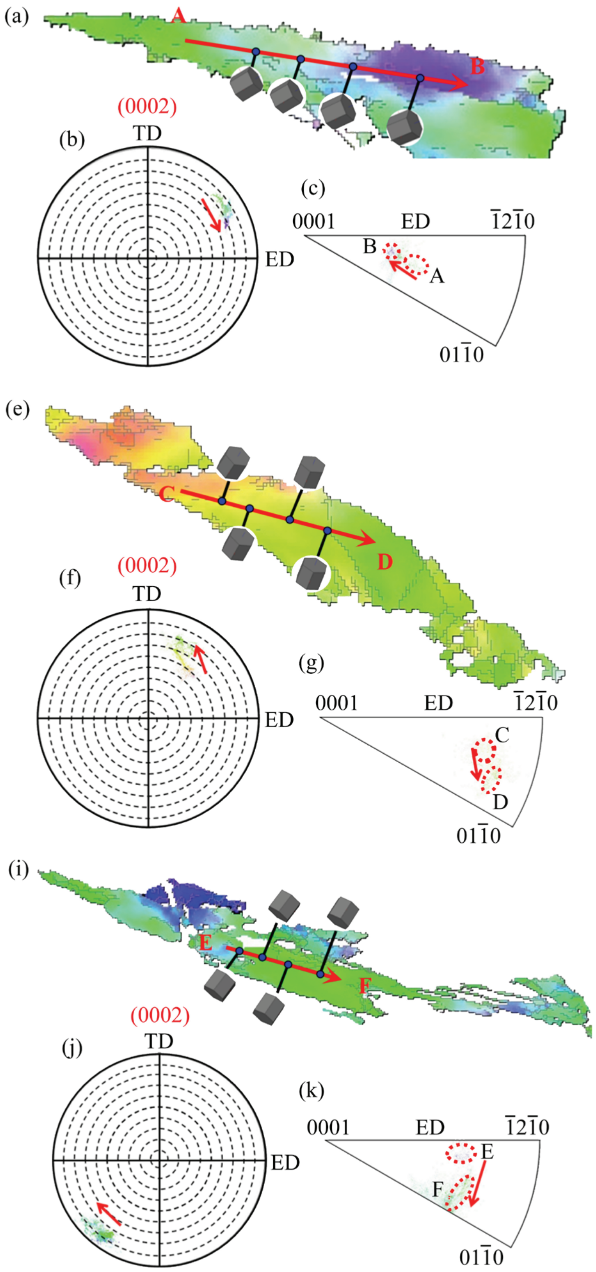

Fig. 9 Details of DRX behavior and corresponding effects on grain orientation in typical grains of G1 (a−d), G2 (e−h), and G3 (i−l) selected in Fig. 5(a): (a, e, i) Inverse pole figure; (b, f, j) (0001) pole figures; (c, g, k) Inverse pole figures along ED; (d, h, l) Misorientation angle developing along red arrow

grains. As strain increases, these LAGBs can trap more movable dislocations and then gradually increase the misorientation within the grains to form HAGBs, which ultimately transform the subgrain into new recrystallized grains, i.e., CDRX mechanisms [25]. Therefore, during further deformation, the larger, elongated grains can generate DRXed grains with different orientations from the parent grains through the CDRX mechanism. G2 and G3 show CDRX characteristics similar to G1.

The G1, G2, and G3 exhibit different grain orientations during deformation due to non-uniform stress distribution during RUE, resulting in varying stresses on grains located at different positions. The non-uniform stress on each grain makes the grain boundary slip or shear deform, thus forming a grain boundary extension line extending into the grain. A large number of dislocations gather at the grain boundary extension line to form a dislocation wall. With increasing deformation, the misorientation near the dislocation wall rapidly increases to normal

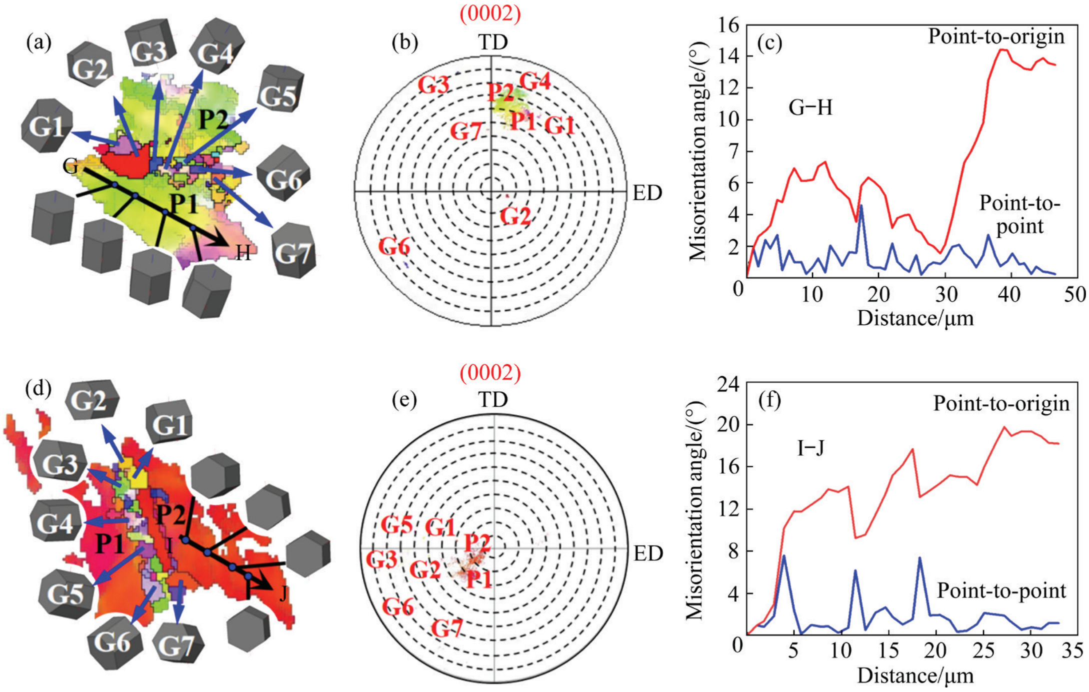

Fig. 10 Details of DRX behavior and corresponding effects on grain orientation in typical regions of R1 (a−c) and R2 (d−f) selected in Figs. 5(a, b): (a, d) Inverse pole figure; (b, e) (0002) pole figures; (c, f) Misorientation angle developing along black arrow

grain boundary misorientation, forming a new grain structure and thus inducing a continuous reaction [26]. There are many LAGBs running through deformed grains in G2 and G3. It can be seen from Fig. 9(h) that misorientation distribution displays a peak value, which is caused by the large misorientation at both ends when crossing the LAGBs. In addition, the misorientation undergoes a process of decrease, as shown in Fig. 9(d). The misorientation along the AB direction increases gradually at first and then enters the purple region, where the misorientation starts to decrease. XIE et al [27] noted that the significant fluctuation of accumulated misorientation is due to the division of deformed grains by geometrically necessary boundaries (GNBs). Furthermore, it was also reported that the obvious change in lattice orientation is related to the growth of parallel microstrips, and the change in microstrip direction can lead to an erroneous reduction in the accumulated misorientation in coarse grains.

In order to further analyze the DRX behavior in coarse grains, the R1 and R2 regions in Figs. 5(a, b) are selected for the microstructure analysis, as shown in Fig. 10. About 58% of the LAGBs are distributed in the R1 region, indicating that a large number of dislocations accumulate in the R1 region. The parent grains, P1 and P2, are irregular in shape, and some DRXed grains (G1−G7) are formed between P1 and P2. LAGBs can absorb free dislocations, transform into HAGBs, and finally transform into new DRXed grains. The accumulated misorientation along the direction of Arrow GH continues to increase to about 13° (Fig. 10(c)), indicating that the dislocation density is high and the intragranular orientation is constantly changed, while higher misorientation is accompanied by the CDRX mechanism [28]. CDRX refers to the cross-slip of dislocations on the non-basal plane, and the screw dislocations in the cross-slip process evolve into edge dislocations, which easily climb along the non-basal plane [29]. Therefore, the LAGBs near the P1 and P2 boundaries are formed by dislocation rearrangement caused by cross-slip and climb.

It can be clearly seen from Fig. 10(b) that there is a certain orientation angle between some CDRXed grains and the parent grains, which weakens the texture intensity to a certain extent. The DRX behavior of Region R2 is similar to that of Region R1. In Fig. 10(f), there are many peaks in the point-to-point misorientation curve along the direction of Arrow IJ. According to reports, this phenomenon occurs because the deformed grains are separated into different orientation bands by GNBs to adapt to the misorientation in the grains [30]. Therefore, CDRX is the main mechanism of DRX during RUE deformation.

3.4 Hardness

Hardness is a comprehensive index to measure the mechanical properties of materials, such as plasticity and strength. The hardness chart of the AZ31 alloy after different deformation temperatures is presented in Fig. 11. It is obvious that after RUE deformation, the hardness of the Mg alloy samples is greatly improved. The hardness of the alloy is about three times its yield strength. For Mg alloys, the relationship between the yield strength and the grain size is as follows: $\sigma_{0.02}=30+0.17d^{-1/2}$ [31]. Therefore, fine-grained strengthening is an effective method to improve the hardness of alloys. Furthermore, Mg alloys have a higher Taylor index than other types of alloys, so grain refinement has a stronger strengthening effect on them [32].

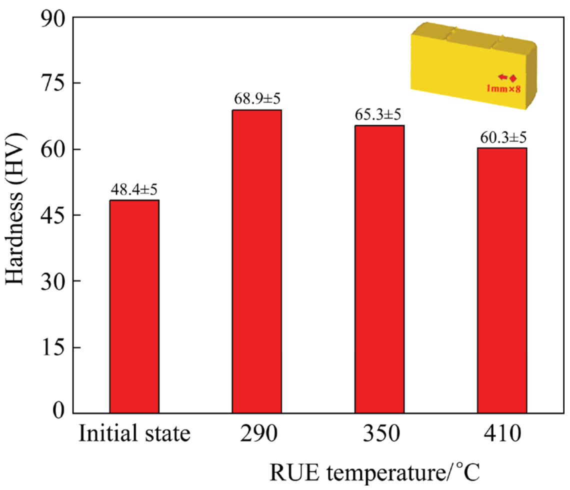

Fig. 11 Hardness of AZ31 alloy at initial state and after RUE deformation at different temperatures

It is worth noting that the hardness of the AZ31 Mg alloy after RUE deformation at 290 °C is the highest, HV 68.9, which is 42.4% higher than that at the initial state. This is because there is not only fine-grained strengthening but also dislocation strengthening at this temperature. At 290 °C, the microstructure contains numerous dislocations, and the geometric dislocation density reaches $1.30\times10^{14}\ \mathrm{m}^{-2}$ (Fig. 6(e)). This can cause basal slip or non-basal slip to be activated, driving the intersection and stacking of dislocations, which results in dislocation entanglements, dividing the grains into lots of small regions, impeding the movement of dislocations in the low dislocation density region of the grains, and then creating the cell structure within the grains [33,34]. According to LI et al [35], increasing the dislocation density can prevent the movement of the newly formed dislocations, thus producing additional hardening effect. Dislocations can be hindered from moving by increasing the dislocation density and generating cell structures, or sub-grains, which have a beneficial impact on the hardness of the alloy.

4 Conclusions

(1) RUE deformation can refine the grain size to 0.8 μm, and the dynamically recrystallized grains primarily nucleate and develop via a CDRX mechanism.

(2) The basal plane parallel to shearing plane texture with a strength of 6.1 is formed at 290 °C, and the $\{11\bar{2}0\}\langle10\bar{1}0\rangle$ texture component is formed at 350 °C. Due to different slip modes and specially oriented grains, the $\{0001\}\langle10\bar{1}0\rangle$ and $\{0001\}\langle11\bar{2}0\rangle$ texture components are formed at 410 °C. The combined action of dislocation slip of basal $\langle a\rangle$ and pyramidal $\langle a\rangle$ is the main cause of base texture split.

(3) After RUE deformation, the hardness of AZ31 Mg alloy significantly increases to HV 68.9, which is 42.4% higher than that at the initial state, attributed to fine-grained strengthening and dislocation strengthening.

CRediT authorship contribution statement

Yu-tian FAN: Data curation, Formal analysis, Investigation, Software, Supervision, Writing − Original draft, Validation, Writing − Review & editing; **Li-wei LU:** Conceptualization, Investigation, Methodology, Project administration, Resources, Validation, Writing − Review & editing; **Jian-bo LIU:** Data curation, Formal analysis, Investigation, Software; **Min MA:** Investigation, Methodology, Project administration; **Wei-ying HUANG:** Investigation, Methodology, Resources; **Rui-zhi WU:** Writing − Review & editing, Visualization, Project administration, Investigation.

Declaration of competing interest

The authors declare that they have no known competing financial interests or personal relationships that could have appeared to influence the work reported in this paper.

Acknowledgments

This work was supported by the National Natural Science Foundation of China (Nos. 52174362, 51975207), Natural Science Foundation of Hunan Province, China (No. 2023JJ10020), Xiangtan Special Project for Building a National Innovative City, China (No. CG-YB20221043), and Yancheng “Talent Plan of Yellow Sea Pearl” for Leading Talent Project, China.

References

[1] MIAO Hong-wei, HUANG Hua, FAN Shi-hao, TAN Jin-yun, WANG Zhong-chang, DING Wen-jiang, YUAN Guang-yin. Nanoscale precipitations in deformed dilute alloying Mg−Zn−Gd alloy [J]. Materials & Design, 2020, 196: 109122.

[2] KANG Wei, LU Li-wei, FENG Long-biao, LU Feng-chi, GAN Chun-lei, LI Xiao-hui. Effects of pre-aging on microstructure evolution and deformation mechanisms of hot extruded Mg−6Zn−1Gd−1Er Mg alloys [J]. Journal of Magnesium and Alloys, 2023, 11(1): 317−328.

[3] FAKHAR N, SABBAGHIAN M. Hot shear deformation constitutive analysis of fine-grained ZK60 Mg alloy sheet fabricated via dual equal channel lateral extrusion and sheet extrusion [J]. Transactions of Nonferrous Metals Society of China, 2022, 32(8): 2541−2556.

[4] DU Qing-lin, LI Chang, CUI Xiao-hui, KONG C, YU Hai-liang. Fabrication of ultrafine-grained AA1060 sheets via accumulative roll bonding with subsequent cryorolling [J]. Transactions of Nonferrous Metals Society of China, 2021, 31(11): 3370−3379.

[5] DOBATKIN S V, ROKHLIN L L, LUKYANOVA E A, MURASHKIN M Y, DOBATKINA T V, TABACHKOVA N Y. Structure and mechanical properties of the Mg−Y−Gd−Zr alloy after high pressure torsion [J]. Materials Science and Engineering A, 2016, 667: 217−223.

[6] HUANG Hao, ZHANG Jing. Microstructure and mechanical properties of AZ31 magnesium alloy processed by multi-directional forging at different temperatures [J]. Materials Science and Engineering A, 2016, 674: 52−58.

[7] HE Shu-heng, WANG Ce, SUN Chao, ZHANG Yue, YAN Kai, JIANG Jing-hua, BAI Jing, XUE Feng, LIU Huan. Corrosion properties of ECAP-processed Mg−Al−Ca−Mn alloys with separate Al2Ca and Mg2Ca phases [J]. Transactions of Nonferrous Metals Society of China, 2022, 32(8): 2527−2540.

[8] WANG Qu-dong, MU Yong-liang, LIN Jin-bao, ZHANG Li, ROVEN H J. Strengthening and toughening mechanisms of an ultrafine grained Mg−Gd−Y−Zr alloy processed by cyclic extrusion and compression [J]. Materials Science and Engineering A, 2017, 699: 26−30.

[9] CHENG Wei-li, TIAN Liang, MA Shi-chao, BAI Yang, WANG Hong-xia. Influence of equal channel angular pressing passes on the microstructures and tensile properties of Mg−8Sn−6Zn−2Al alloy [J]. Materials, 2017, 10(7): 708.

[10] JI Jin-sheng, ZHENG Jie, SHI Yu-sha, ZHANG Heng, ZHANG Zhi-min, XUE Yong. Reinforcing effects of cyclic expansion extrusion with an asymmetrical extrusion cavity (CEE-AEC) on pure magnesium [J]. Materials Research Express, 2021, 8(5): 056502.

[11] SIAHSARANI A, SAMADPOUR F, MORTAZAVI M H, FARAJI G. Microstructural, mechanical and corrosion properties of AZ91 magnesium alloy processed by a severe plastic deformation method of hydrostatic cyclic expansion extrusion [J]. Metals and Materials International, 2021, 27(8): 2933−2946.

[12] XIE Jin-shu, ZHANG Zhi, LIU Shu-juan, ZHANG Jing-huai, WANG Jun, HE Yu-ying, LU Li-wei, JIAO Yun-lei, WU Rui-zhi. Designing new low alloyed Mg-RE alloys with high strength and ductility via high-speed extrusion [J]. International Journal of Minerals, Metallurgy and Materials, 2023, 30(1): 82−91.

[13] KRAJŇÁK T, MINÁRIK P, STRÁSKÁ J, GUBICZA J, DLUHOŠ L, MÁTHIS K, JANEČEK M. Influence of temperature of ECAP processing on the microstructure and microhardness of as-cast AX41 alloy [J]. Journal of Materials Science, 2020, 55(7): 3118−3129.

[14] LU Li-wei, LIU Chu-ming, ZHAO Jun, ZENG Wen-bing, WANG Zhong-chang. Modification of grain refinement and texture in AZ31 Mg alloy by a new plastic deformation method [J]. Journal of Alloys and Compounds, 2015, 628: 130−134.

[15] WU S K, CHOU T S, WANG J Y. The deformation textures in an AZ31B magnesium alloy [J]. Materials Science Forum, 2003, 419/420/421/422: 527−532.

[16] KRAJŇÁK T, MINÁRIK P, GUBICZA J, MÁTHIS K, KUŽEL R, JANEČEK M. Influence of equal channel angular pressing routes on texture, microstructure and mechanical properties of extruded AX41 magnesium alloy [J]. Materials Characterization, 2017, 123: 282−293.

[17] TIAN Ye, HU Hong-jun, ZHAO Hui, ZHANG Wei, LIANG Peng-cheng, JIANG Bin, ZHANG Ding-fei. An extrusion−shear−expanding process for manufacturing AZ31 magnesium alloy tube [J]. Transactions of Nonferrous Metals Society of China, 2022, 32(8): 2569−2577.

[18] JIANG M G, YAN H, CHEN R S. Microstructure, texture and mechanical properties in an as-cast AZ61 Mg alloy during multi-directional impact forging and subsequent heat treatment [J]. Materials & Design, 2015, 87: 891−900.

[19] EBRAHIMI M, WANG Qu-dong, ATTARILAR S. A comprehensive review of magnesium-based alloys and composites processed by cyclic extrusion compression and the related techniques [J]. Progress in Materials Science, 2023, 131: 101016.

[20] LI Xiao-qiang, LE Qi-chi, LI Dan-dan, WANG Ping, JIN Pei-peng, CHENG Chun-long, CHEN Xing-rui, REN Liang. Hot tensile deformation behavior of extruded LAZ532 alloy with heterostructure [J]. Materials Science and Engineering A, 2021, 801: 140412.

[21] YAN Zhi-feng, WANG Deng-hui, HE Xiu-li, WANG Wen-xian, ZHANG Hong-xia, DONG Peng, LI Chen-hao, LI Yu-li, ZHOU Jun, LIU Zhuang, SUN Li-yong. Deformation behaviors and cyclic strength assessment of AZ31B magnesium alloy based on steady ratcheting effect [J]. Materials Science and Engineering A, 2018, 723: 212−220.

[22] CHE Bo, LU Li-wei, ZHANG Jia-long, ZHANG Jing-huai, MA Min, WANG Li-fei, QI Fu-gang. Effects of cryogenic treatment on microstructure and mechanical properties of AZ31 magnesium alloy rolled at different paths [J]. Materials Science and Engineering A, 2022, 832: 142475.

[23] BISWAS S, BEAUSIR B, TOTH L S, SUWAS S. Evolution

of texture and microstructure during hot torsion of a magnesium alloy [J]. Acta Materialia, 2013, 61(14): 5263−5277.

[24] LIAO Qi-yu, JIANG Yan-chao, LE Qi-chi, CHEN Xing-rui, CHENG Chun-long, HU Ke, LI Dan-dan. Hot deformation behavior and processing map development of AZ110 alloy with and without addition of La-rich Mish Metal [J]. Journal of Materials Science & Technology, 2021, 61: 1−15.

[25] WEI Qing-he, YUAN Lin, MA Xiao, ZHENG Ming-yi, SHAN De-bin, GUO Bin. Strengthening of low-cost rare earth magnesium alloy Mg−7Gd−2Y−Zn−0.5Zr through multi-directional forging [J]. Materials Science and Engineering A, 2022, 831: 142144.

[26] CHEN Qing-hua, CHEN Rui-nan, SU Jian, HE Qing-song, TAN Bin, XU Chao, HUANG Xu, DAI Qing-wei, LU Jian. The mechanisms of grain growth of Mg alloys: A review [J]. Journal of Magnesium and Alloys, 2022, 10(9): 2384−2397.

[27] XIE Bing-chao, ZHANG Bao-yun, NING Yong-quan, FU M W. Mechanisms of DRX nucleation with grain boundary bulging and subgrain rotation during the hot working of nickel-based superalloys with columnar grains [J]. Journal of Alloys and Compounds, 2019, 786: 636−647.

[28] PAN Xiao-huan, WANG Li-fei, LU Peng-bin, ZHANG Hua, HUANG Guang-sheng, ZHENG Liu-wei, XING Bin, CHENG Wei-li, WANG Hong-xia, LIANG Wei, SHIN K S. Unveiling the planar deformation mechanisms for improved formability in pre-twinned AZ31 Mg alloy sheet at warm temperature [J/OL]. Journal of Magnesium and Alloys (2022). https://doi.org/10.1016/j.jma.2022.11.010.

[29] PAN Xiao-huan, WANG Li-fei, XUE Liang-liang, SABBAGHIAN M, LU Peng-bin, WU Wei, HUANG Guang-sheng, XING Bin, WANG Hong-xia. Dynamic recrystallization, twinning behaviors and mechanical response of pre-twinned AZ31 Mg alloy sheet along various strain paths at warm temperature [J]. Journal of Materials Research and Technology, 2022, 19: 1627−1649.

[30] CHE Bo, LU Li-wei, WU Zhi-qiang, ZHANG Hua, MA Min, LUO Jun, ZHAO Hong-mei. Dynamic recrystallization behavior and microstructure evolution of a new Mg−6Zn−1Gd−1Er alloy with and without pre-aging treatment [J]. Materials Characterization, 2021, 181: 111506.

[31] YOSHIDA Y, CISAR L, KAMADO S, KOJIMA Y. Effect of microstructural factors on tensile properties of an ECAE-processed AZ31 magnesium alloy [J]. Materials Transactions, 2003, 44(4): 468−475.

[32] ZENG Xiao-qin, ZHU Qing-chun, LI Yang-xin, DING Wen-jiang. Second phase particle strengthening in magnesium alloys [J]. Materials China, 2019, 38(3): 109−204.

[33] JIA Jian-bo, XU Yan, YANG Yue, CHEN Chen, LIU Wen-chao, HU Lian-xi, LUO Jun-ting. Microstructure evolution of an AZ91D magnesium alloy subjected to intense plastic straining [J]. Journal of Alloys and Compounds, 2017, 721: 347−362.

[34] FAN Yu-tian, LU Li-wei, ZHOU Tao, ZHANG Hua, QI Fugang, MA Min, WU Zhi-qiang, JIA Wei-tao, ZHANG Sha, HUANG Wei-ying. Improvement of the microstructure and microhardness of AQ80 magnesium alloy by repeated upsetting-extrusion [J]. Metals and Materials International, 2023, 29: 3052−3065.

[35] LI Jing-ren, XIE Dong-sheng, YU Han-song, LIU Ruo-lin, SHEN Yang-zi, ZHANG Xing-shuo, YANG Chang-lin, MA Li-feng, PAN Hu-cheng, QIN Gao-wu. Microstructure and mechanical property of multi-pass low-strain rolled Mg−Al−Zn−Mn alloy sheet [J]. Journal of Alloys and Compounds, 2020, 835: 155228.

变形温度对塑性变形新方法加工的 AZ31 镁合金显微组织和织构的影响

范宇田[1]，卢立伟[1,2]，刘剑波[1]，马 旻[1,2]，黄伟颖[2,3]，巫瑞智[2,4]

1. 湖南科技大学 材料科学与工程学院，湘潭 411201；
2. 湖南金峰机械科技有限公司，娄底 417700；
3. 长沙理工大学 能源与动力工程学院，高效清洁能源利用重点实验室，长沙 410114；
4. 哈尔滨工程大学 材料科学与化学工程学院，超轻材料与表面技术教育部重点实验室，哈尔滨 150001

摘　要：提出一种新的反复镦挤变形(RUE)方法。采用光学显微镜(OM)、X 射线衍射(XRD)、电子背散射衍射(EBSD)和维氏硬度计分析不同变形温度对 RUE 变形 AZ31 镁合金显微组织和织构的影响。结果表明：经 RUE 变形后，AZ31 镁合金组织局部细化至 0.8 μm，细化机制主要为连续动态再结晶(CDRX)；随着温度的升高，首先形成平行于剪切面的基面织构，随后形成强度减弱的 $\{11\bar{2}0\}\langle10\bar{1}0\rangle$ 织构，最后形成 $\{0001\}\langle10\bar{1}0\rangle$ 和 $\{0001\}\langle11\bar{2}0\rangle$ 织构。基面和锥面$\langle a\rangle$位错滑移导致织构分裂。经 RUE 变形后 AZ31 镁合金的最大硬度较初始状态提高 42.4%，主要原因是细晶强化和位错强化。

关键词：AZ31 镁合金；反复镦挤变形；动态再结晶；织构；硬度

(Edited by Bing YANG)